Supporting Information

A Zundel Ion in the Catalytic Proton Transfer Pathway of [FeFe]-Hydrogenase

Lingling Liu[1], Max A. Klamke[2], Federica Arrigoni[3], Oliver Lampret[1], Julian Kleinhaus[4], Ulf-Peter Apfel[4,5], Eckhard Hofmann[6], Claudio Greco[7], Thomas Happe[1], Sven T. Stripp[2]*, Jifu Duan[1]*

[1] Photobiotechnology group, Faculty of Biology and Biotechnology, Ruhr University Bochum, Universitätsstrasse 150, 44801 Bochum, Germany

[2] Institute of Chemistry, Spectroscopy & Biocatalysis, University of Potsdam, Karl-Liebknecht- Straße 24-25, 14476 Potsdam, Germany

[3] Department of Biotechnology and Biosciences, University of Milano-Bicocca, Piazza della Scienza 2, 20126, Milan, Italy

[4] Inorganic Chemistry I, Faculty of Chemistry and Biochemistry, Ruhr University Bochum, Universitätsstrasse 150, 44801 Bochum, Germany

[5] Department of Energy, Electrosynthesis Group, Fraunhofer UMSICHT, 46047 Oberhausen, Germany

[6] Protein Crystallography, Faculty of Biology and Biotechnology, Ruhr University Bochum, Universitätsstrasse 150, 44801 Bochum, Germany

[7] Department of Earth and Environmental Sciences, University of Milano-Bicocca, Piazza della Scienza 1, 20126 Milan, Italy

Correspondence: jifu.duan@ruhr-uni-bochum.de, sven.stripp@uni-potsdam.de.

Contents

Experimental section

Protein preparation

Site directed mutagenesis (SDM) was applied to introduce the desired amino acid substitutions at specific sites.[1] QuikChange PCR (polymerase chain reaction) was performed using the mismatching primers listed in **Table S1**. The sequences of resulting constructs were confirmed before using for protein expression. After transformation of *E. coli* strain BL21(DE3)Δ*iscR* by electroporation with *Cr*HydA1 and *Cp*I-encoding plasmids,[2] apo-forms of *Cr*HydA1 and *Cp*I lack of $[2Fe]_H$ were overexpressed by following previous protocol.[3] All steps for protein harvest and purification were performed under strict anaerobic conditions, as previously described.[4] 2 mM sodium dithionite (NaDT) was routinely included as supplement in 0.1 M tris-HCl buffer for protein preparation. However, for samples used for results of **Figure 3** and **Figures S5-S10**, NaDT was strictly excluded in all the protein preparation steps. The Strep-Tactin affinity chromatography was applied for protein purification. The eluted proteins were subsequently concentrated using Amicon concentrator (Amicon Ultra-4, 30 KDa, Merck Millipore) by centrifuge.

In vitro maturation and activity assays

The $[2Fe]_H$ mimics was synthesized following previous protocol.[5] Fully active holo-form hydrogenases were obtained using *in vitro* maturation.[6] H_2 evolution assay was carried out in 8 ml air-tight Suba vessels. The total reaction volume was 2 ml K_2HPO_4/KH_2PO_4 buffer (pH 6.8) with 100 mM NaDT as electron donor and 10 mM methyl viologen as electron mediator. After adding 400 ng holo-*Cp*I protein, vessels were sealed by rubber lids immediately and purged with argon for 5 min. Then vessels were shaken in 37 °C water bath for 20 min. Afterwards, 400 µl headspace from each vessel were injected into gas chromatography to quantify the amount of produced hydrogen and determine activity of enzyme. For pH-dependent activity assay, all the steps were the same except replacing the K_2HPO_4/KH_2PO_4 pH 6.8 buffer with different buffers from pH 5–9. The range of buffers included: pH 5–6.5 (200 mM MES-NaOH, 2-(N-morpholino) ethanesulfonic acid) (Roth); pH 7–7.5 (200 mM MOPS-NaOH, 3-(N-morpholino) propanesulfonic acid); pH 8–9 (200 mM Tris–HCl) (Sigma-Aldrich); and pH 10 (200 mM CAPS-NaOH, N-cyclohexyl-3- aminopropanesulfonic acid) (Roth).

Protein film electrochemistry

Protein film electrochemistry experiments were performed using a gas-tight electrochemical cell under strictly anoxic conditions. The potentials were controlled using a PalmSens potentiostat (PalmSens 4) and program PStrace 5.8. The temperature was kept at 10 °C by a water jacket. A hydrogen gas tube with adjustable flow rate was connected to the cell to provide 100 % H_2 for H_2 oxidation measurements. A pyrolytic graphite edge rotating disk electrode was used as a working electrode and connected to a rotator that was set to a constant speed of 3000 rpm. The reference electrode (Ag/AgCl) was filled with 3 M KCl and the potential was corrected using the equation: $E_{SHE} = E_{Ag/AgCl} + 0.217$ V at 10 °C. A platinum wire was used as the counter-electrode. A 2–4 µl sample of holo [FeFe]-hydrogenase (approximately 10 µM) was applied on the pre-polished working electrode. After incubation for 2–4 min, the working

electrode was rinsed with water to remove unbound protein molecules. All experiments were conducted using a "mixed buffer" (15 mM MES, HEPES, sodium acetate, TAPS, and CHES, supplemented with 0.1 M NaCl, and adjusted with HCl or NaOH to pH values 5–9).[7]

The cyclic voltammograms (CVs) of wild-type *Cp*I at pH 5–9 are shown below (**Fig S0**). For **Figure S3**, forward and backward scan are averaged and the current of each CV is normalized to the respective maximum reducing potential at E = -780 mV + 60 mV · (9-x) where x is the pH value of the electrolyte buffer. We chose pH 9 as reference because the current becomes stable at approximately -780 mV vs. SHE (*). This normalization aids the comparison with the variants (**Figure S3**). In the measured potential window, we did not observe high potential inactivation, which typically occurs at $E_{inact} > 0$ mV. [8–10]

Figure S0. Cyclic voltammograms of wild-type *Cp*I (not normalized)

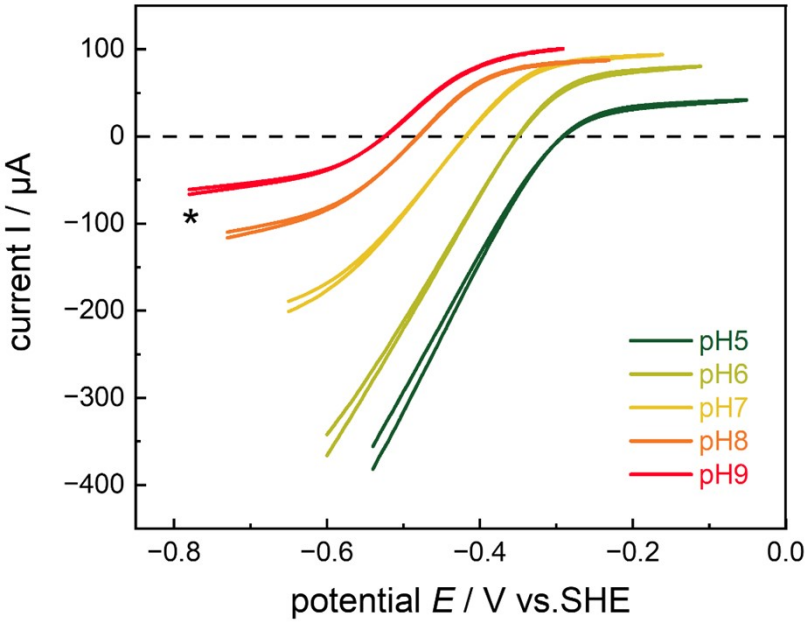

Infrared spectroscopy

The FTIR spectrometer (Bruker GmbH) was equipped with a ZnSe/Si crystal ATR cell and placed in the anaerobic tent. Infrared spectra were recorded in 80 kHz scanning velocity at a spectral resolution of 2 cm^{-1} from 1000 to 4000 cm^{-1}.[11] The measurements were performed at room temperature. The MTC (mercuric cadmium-telluride) detector was continuously cooled with liquid nitrogen. The protein samples in the concentrations of 0.5-1 mM were applied on the ATR crystal. To enrich H_{ox} state, the samples were flushed with N_2 of flow rate of 3 L/min f controlled by mass flow controllers (Sierra Instruments). The data were recorded as pH 8 buffer free of NaDT. Afterwards, 4 µl pH 4 0.1 M Mes-NaOH buffer was added on the crystal to rehydrate the same protein film. Flushing with dry N_2 was repeated as above. The measurement persisted until the peaks were stable for at least 20 min. The data was recorded

as pH 4 buffer free NaDT. As for the control experiments with NaDT as the reductant, 4 µl pH 4.0 0.1 M Mes-NaOH buffer with 10 mM NaDT was used.

FTIR spectra in the CO/CN regime of the H-cluster were cut and corrected for the background contribution of liquid H_2O by the rubber band correction tool in OPUS. Second derivative spectra of unmodified absorbance spectra were computed to verify the peak position of each band. Band fitting was performed using custom software tool GloFit. First, the CO/CN pattern of H_{ox} and $H_{ox}H$ was extracted from spectra showing pure states (frequency, intensity, FWHM). Spectra with mixed populations were described with H_{ox} and $H_{ox}H$ first before the remaining bands were fitting manually to $H_{red'}$ and $H_{red'}H$ according to the known trends[12] in band position (**Figure S1**).

Protein crystallization

Vapor diffusion hanging drop method was applied under anaerobic condition at 277 K to crystallize *Cp*I-N160L, *Cp*I-Q195L and *Cp*I-N160L-Q195L variants as described previously.[13] 2 µl of 15 mg/ml protein was added into 2 µl crystallization buffer on the cover slip and the cover slip was turned upside down and placed on reservoir. After about one week of crystal growth, crystals were mounted on loops and subject to flash freezing in liquid N_2. Crystals were sent to synchrotron facilities (ESRF and DESY) for diffraction experiment. **Table S3** showed crystallization conditions and beamlines for these three variants. Data were processed using XDS.[14] Phenix, and Coot were used for molecular replacement (starting model was 4XDC) and structural refinement.[15,16] The details of crystallographic data gained for each of the variants were summarized in **Table S4**.

Quantum chemical calculations

DFT calculations were performed using TURBOMOLE 4.1. Geometry optimizations were carried out at the BP86/TZVP level of theory, adding D4 dispersion corrections (a typical scheme used to model hydrogenase-related systems.[17–20] The Resolution-of-Identity (RI) technique was used to enhance computational efficiency.[21] calculations were carried out on QM-cluster model was constructed based on the *Cp*I [FeFe]-hydrogenase structure (PDB ID: 4XDC), comprising 161 atoms. The QM-cluster model was constructed based on the *Cp*I [FeFe]-hydrogenase structure (PDB ID: 4XDC) and comprised 161 atoms. It included residues directly involved in H-bonding with the CN^- ligands, as well as residues along the proton transfer path (PTP, both those directly participating in proton transfer and those interacting with or stabilizing the two conserved water molecules), similarly to previous investigations focused on this specific PTP region (see **Figure S10** for further details).[22] Optimizations, performed with strategic constraints applied to preserve crystallographic positions and mitigate artifacts from the absence of the full protein matrix, were followed by full vibrational analysis. As expected for constrained models of this complexity, a few low-intensity imaginary frequencies (<100 cm^{-1}) were observed, all of which were deemed spurious artifacts of the applied constraints. To ensure that the observed spectral trends were not functional-dependent, IR frequencies were also computed using TPSS[23], TPSSh[24] and B3LYP[25,26] functionals on BP86-optimized geometries.

Supplementary figures

Figure S1. FTIR signature of H-cluster states $H_{red'}$ and $H_{red'}H$

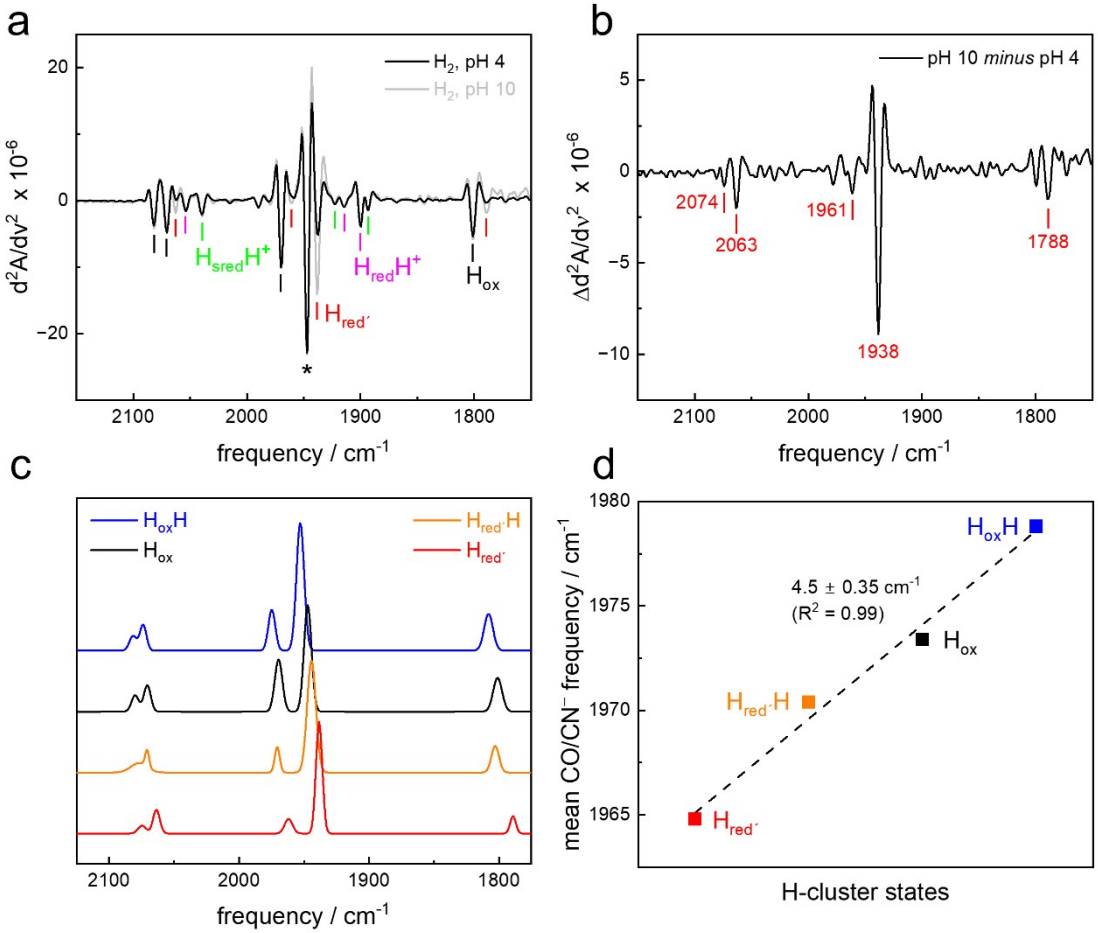

(a) Second derivative spectra of *Cp*I in the presence of 10% H_2 at pH 4 and pH 10 (no NaDT). As shown for *Cr*HydA1 previously,[27] alkaline pH values facilitate accumulating the $H_{red'}$ state (appearing with a higher intensity in the grey spectrum). Spectra a scaled to the intensity of the 1946 cm^{-1} band (*) of the H_{ox} state. **(b)** Subtraction of the second derivative spectra reveals the full signature of $H_{red'}$ in *Cp*I, which is reported here for the first time. Based on $H_{red'}$ and the known signatures of H_{ox} and $H_{ox}H$ in *Cp*I,[12] the elusive $H_{red'H}$ spectrum can be extracted. **(c)** The spectral fits of these four H-cluster states in were used to describe the experimental data in the manuscript. Eventually, panel **(d)** depicts the continuous up-shift of the mean H-cluster frequency (=(νCN1+ νCN2+ νCOp+ νCOd+ νCOμ)/5) from $H_{red'} \rightarrow H_{red'}H \rightarrow H_{ox} \rightarrow H_{ox}H$ by 4.5 cm^{-1}/species. This allows distinguishing $H_{red'}H$ from H_{ox} in complex spectra.

Figure S2. H_2 evolution activities.

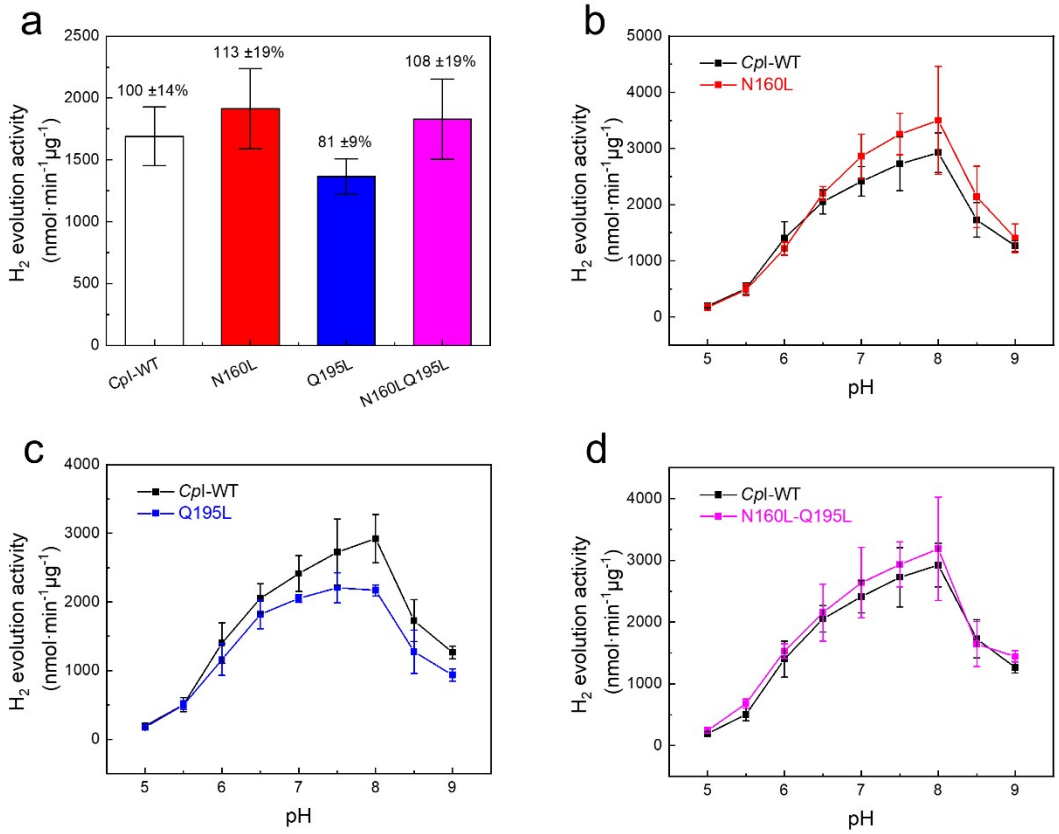

(a) Averaged across all measured pH values (pH 5–9), the mean H_2 evolution activity of wild-type *Cp*I was 1690 ± 235 nmol H_2 x min^{-1} x μg^{-1} (100 ±14%). The mean H_2 evolution activity of *Cp*I variants N160L, Q195L, and N160L-Q195L accounts to 113 ±19%, 81 ±9%, and 108 ±19% of wild-type activity, as indicated in the panels. **(b)–(d)** pH-dependent H_2 evolution activities of *Cp*I variants N160L (red), Q195L (blue), and N160L-Q195L (magenta) as described in the Methods section. The activity profile of wild-type *Cp*I (black) is plotted in each panel for comparison. The Y axis represents absolute H_2 evolution activities (nmol H_2 x min^{-1} x μg^{-1}). Error bars represent standard deviations (n = 3).

Figure S3. Protein film electrochemistry.

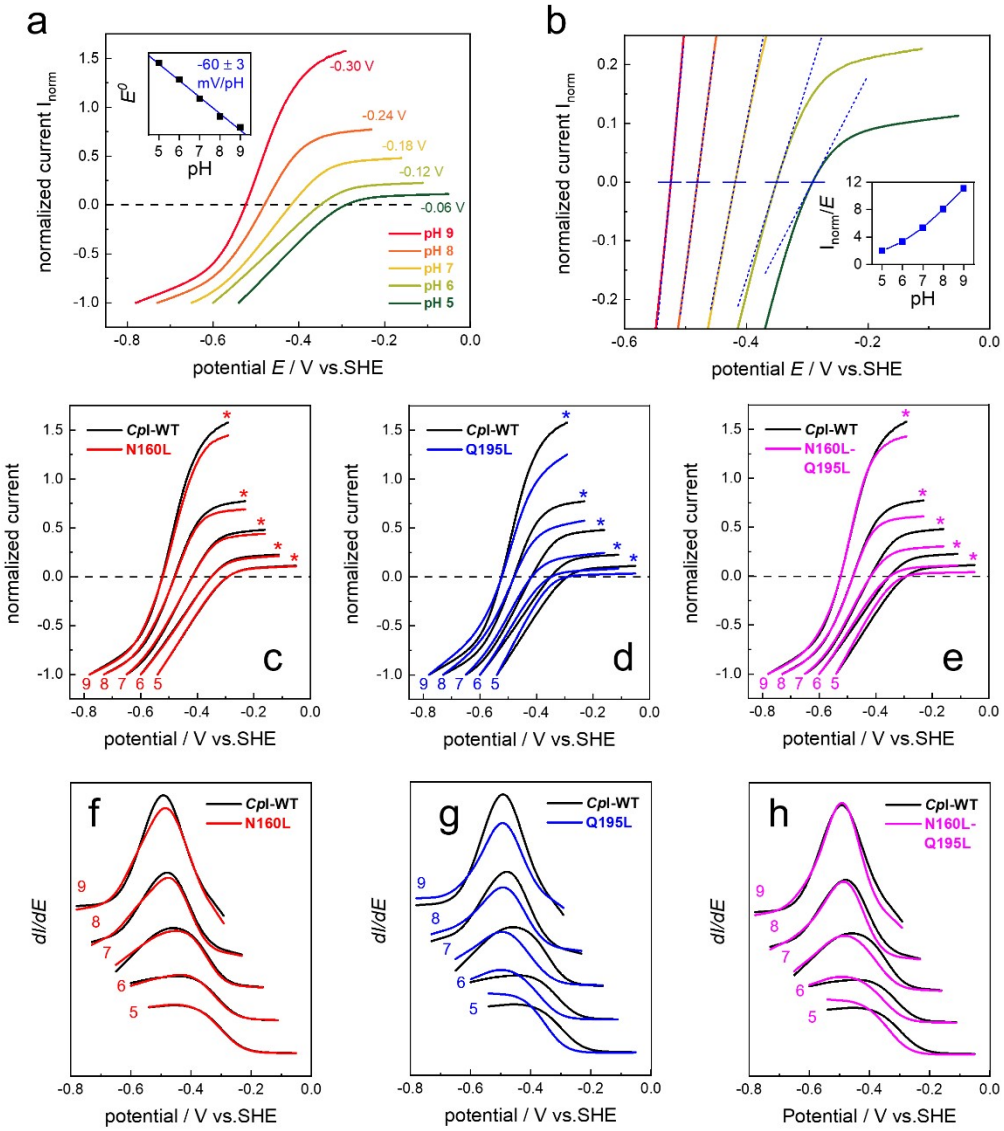

(a) Normalized CV traces for wild-type *Cp*I (100 % H_2, pH 5–9, see **Figure S0** for the original data). The inset shows how the reduction potential E^0 shifts by -60 mV/pH. Potentials at which the maximum H_2 oxidation current is measured are annotated. **(b)** Close-up on the zero-current axis. Here, the slope at I=0 (given by tangential linear regression) suggests an overpotential dependance inversely proportional to pH (inset).[28] **(c)–(e)** Comparison of normalized CV traces of wild-type *Cp*I (black) with *Cp*I-N160L (red), *Cp*I-Q195L (blue) and *Cp*I-N160L-Q195L (magenta). The maximum currents at oxidizing potentials (*) are referenced to wild-type *Cp*I and plotted in **Figure 2b** of the main script. **(f)–(h)** Comparison of first derivative CV traces stacked between pH 9–5 from top to bottom. Variant *Cp*I-N180L shows no meaningful differences compared to wild-type *Cp*I whereas variant *Cp*I-Q195L hints at slower catalysis (*i.e.*, reduced amplitude) and a higher overpotential (*i.e.*, a lower slope at I=0). Double variant *Cp*I-N160L-Q195L displays an intermediate phenotype with a negligible decrease of amplitude and a smaller overpotential increase.

Figure S4. Comparison of structures of *Cp*I-WT and mutants targeting the putative regulatory PTP.

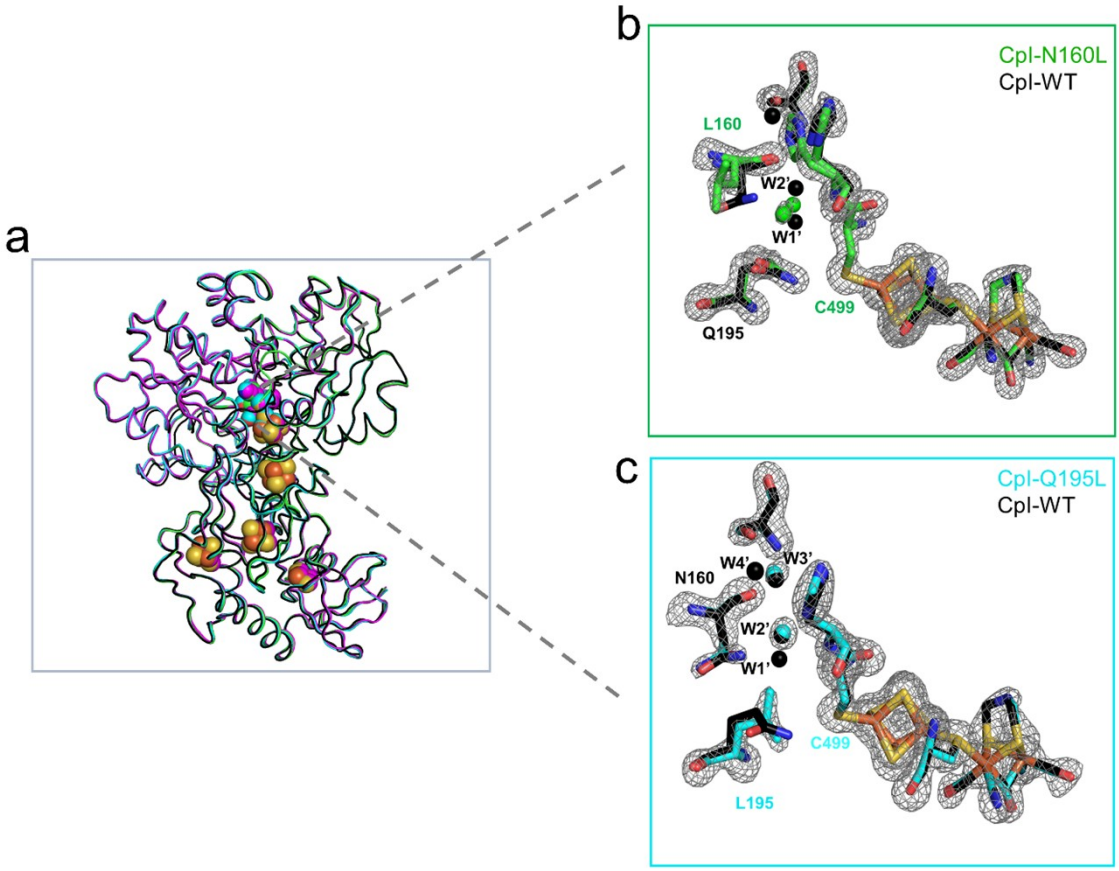

(a) Overall structures of *Cp*I-N160L (green), *Cp*I-Q195L (cyan), *Cp*I-N160L-Q195L (magenta) are superimposed with *Cp*I-WT (PDB: 4XDC, chain B, black). The main chains are showed as cartoon and Fe-S clusters are displayed as spheres. **(b)** and **(c)** are electron density maps that correspond to *Cp*I-N160L (PDB: 9RJ9), *Cp*I-Q195L (PDB: 9RJQ) with stick models after being superimposed with *Cp*I-WT (4XDC) where water molecules and carbon atoms are colored in black. In **(b)** and **(c)**, carbon and oxygen of each structure share the same color for clarity: green, cyan and black for N160L, Q195L and WT respectively. Comparing with WT structure: W1 is present but slightly shifted away from C499 in *Cp*I-N160L; W1 vanished in *Cp*I-Q195L. Simulated annealing omit-maps (Fo-Fc) were contoured at 3 σ for *Cp*I-N160L and *Cp*I-Q195L.

Figure S5. FTIR spectra of *Cp*I-N160L, *Cp*I-Q195L, and *Cp*I-N160-Q195L.

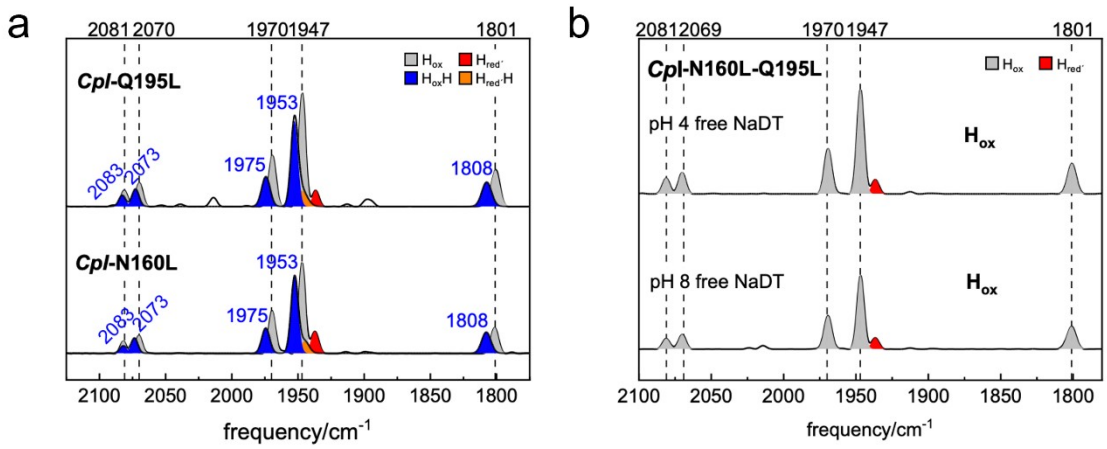

All spectra are normalized at 1540 cm^{-1} of the amide II band ahead of baseline correction. **(a)** For the single variants *Cp*I-Q195L and *Cp*I-N160L, protein samples were measured under N_2 and at two buffer conditions (pH 8 without NaDT and pH 4 with 10 mM NaDT). The later conditions induced conversion into $H_{ox}H$ (blue shading). **(b)** For the double variant *Cp*I-Q195L-N160L, protein samples were measured under N_2 and at pH 4 and pH 8, both buffers free of NaDT. Irrespective of pH value only the H_{ox} state was observed (grey shading). Color code: H_{ox}, grey; $H_{ox}H$, blue; $H_{red'}$, red; $H_{red'}H$, orange.

Figure S6. FTIR spectra of *Cr*HydA1 under various conditions.

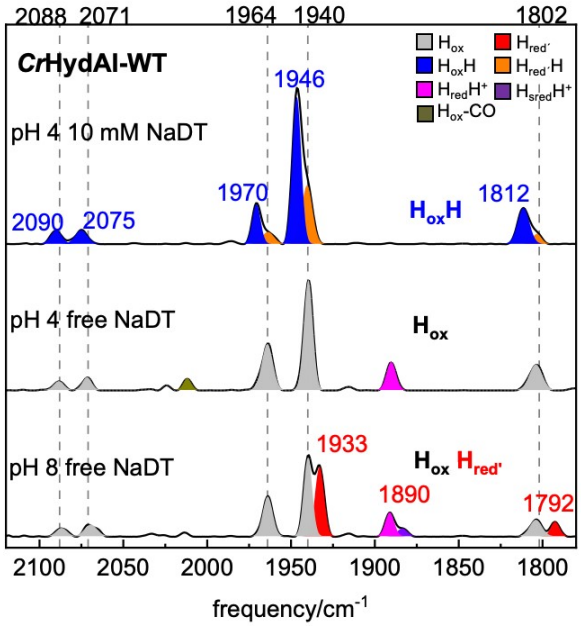

All spectra are normalized at 1540 cm^{-1} of the amide II band ahead of baseline correction. In the presence of 10 mM NaDT at pH 4 and under N_2, wild-type *Cr*HydA1 converts into $H_{ox}H$ (top spectrum, blue shading). Under similar conditions but without NaDT, *Cr*HydA1 remains in the H_{ox} state (grey shading). In the absence of NaDT at pH 8 and under 10% H_2, wild-type *Cr*HydA1 converts into a mixture of $H_{red'}$, $H_{red}H^+$, and $H_{sred}H^+$ (bottom spectrum). Note that H_{hyd} is largely absent here. Color code: H_{ox}, grey; $H_{ox}H$, blue; $H_{red'}$, red; $H_{red'}H$, orange; $H_{red}H^+$, magenta; $H_{sred}H^+$, violet; H_{ox}-CO, brownish.

Figure S7. FTIR spectra of further *Cp*I and *Cr*HydA1 variants.

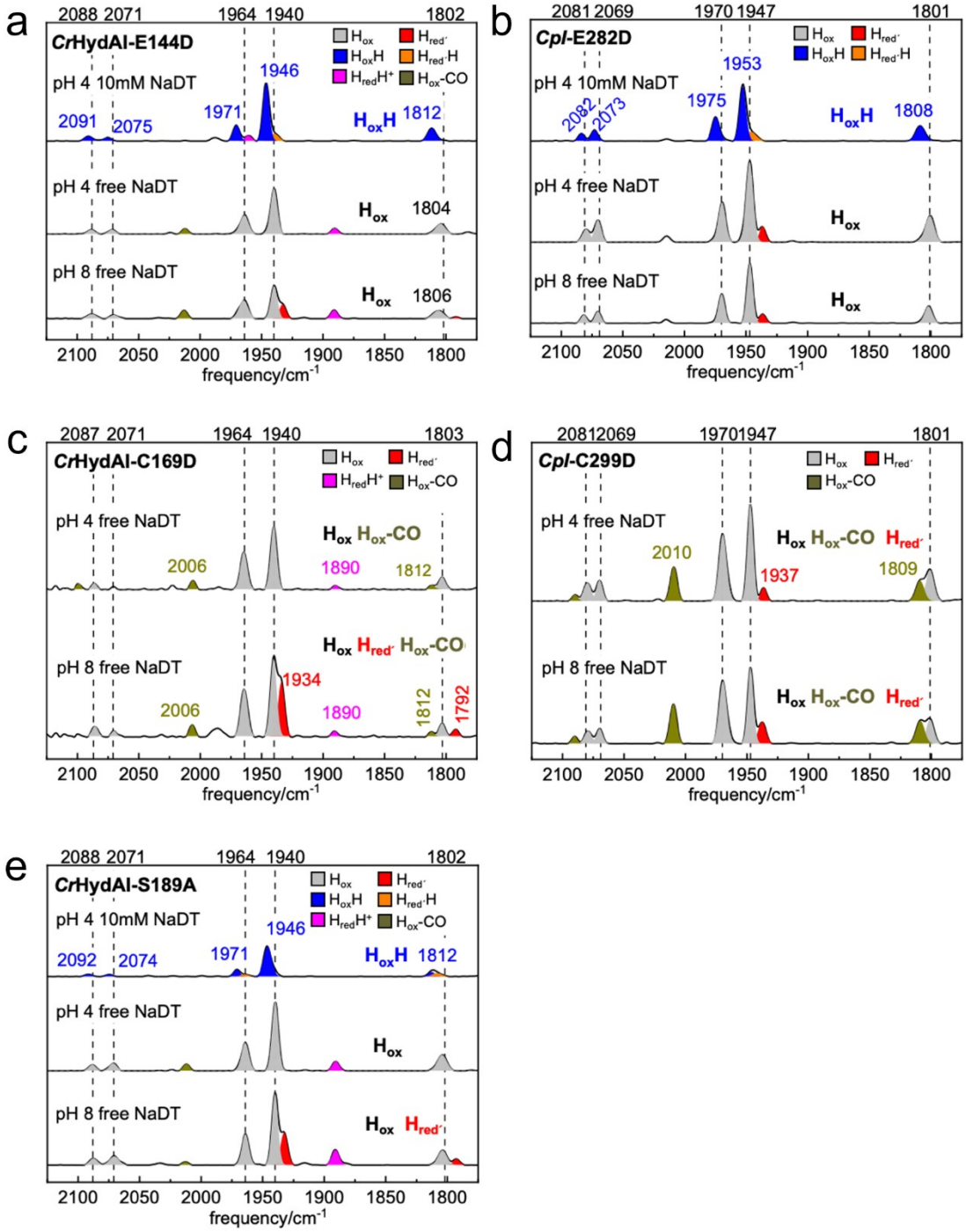

All spectra are normalized at 1540 cm^{-1} of the amide II band ahead of baseline correction. N_2 is used to enrich the oxidized states, further conditions are labeled above each spectrum. The dashed lines show the frequencies of H_{ox} of wild-type *Cr*HydA1 (left column) and *Cp*I (right column). Residues E144 **(a)** and E282 **(b)** as well as C169 **(c)** and C299 **(d)** refer to the same position in *Cr*HydA1 and *Cp*I, respectively. Note that the accumulation of $H_{ox}H$ in *Cr*HydA1-C169D in the presence of NaDT was shown earlier.[12] Color code: H_{ox}, grey; $H_{ox}H$, blue; $H_{red'}$, red; $H_{red'}H$, orange; $H_{red}H^+$, magenta; $H_{sred}H^+$, violet; H_{ox}-CO, brownish.

Figure S8. Dehydration of *Cp*I and *Cp*I-E279D monitored *via* ATR FTIR.

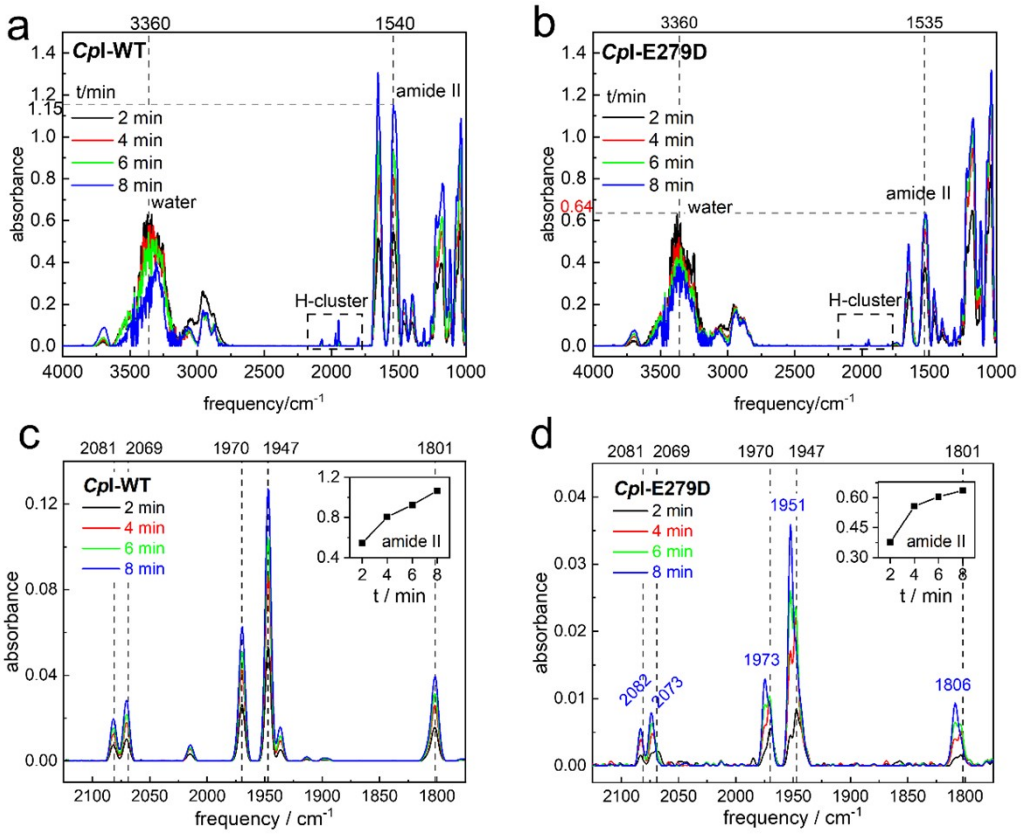

Full ATR FTIR spectra of **(a)** wild-type *Cp*I and **(b)** *Cp*I-E279D (both pH 4, no NaDT) including the OH regime of liquid H_2O (3600–3000 cm^{-1}) and the "amide" regime with the CO and NH vibrations of the protein backbone (amide I and amide II at 1650 and 1540 cm^{-1}, respectively). Below 1350 cm^{-1} the spectra are dominated by buffer contributions. All spectra are background corrected. The depicted time series' show a continuous dehydration of the protein films under water-free N_2, *i.e.*, a decrease of H_2O signals and an increase of amide signals. The latter reflects an increase in protein concentration. Panels **(c)** and **(d)** show the spectra in the H-cluster regime during the drying process for wild-type *Cp*I and *Cp*I-E279D. Despite low pH and the increase in protein concentration, wild-type *Cp*I remains in the H_{ox} state, which is explained by the lack of reductant in the sample.[12] On the opposite, proton transfer pathway variant *Cp*I-E279D clearly shifts toward $H_{ox}H$ upon dehydration, notably in the absence of NaDT. Dehydration has been used to enrich $H_{ox}H$ in sample with less effective reductants previously.[29] The inset in panels **(c)** and **(d)** tracks the changes of amide II intensity at 1540 cm^{-1} versus time.

Figure S9. FTIR spectra of *Cr*HydA1-E141D.

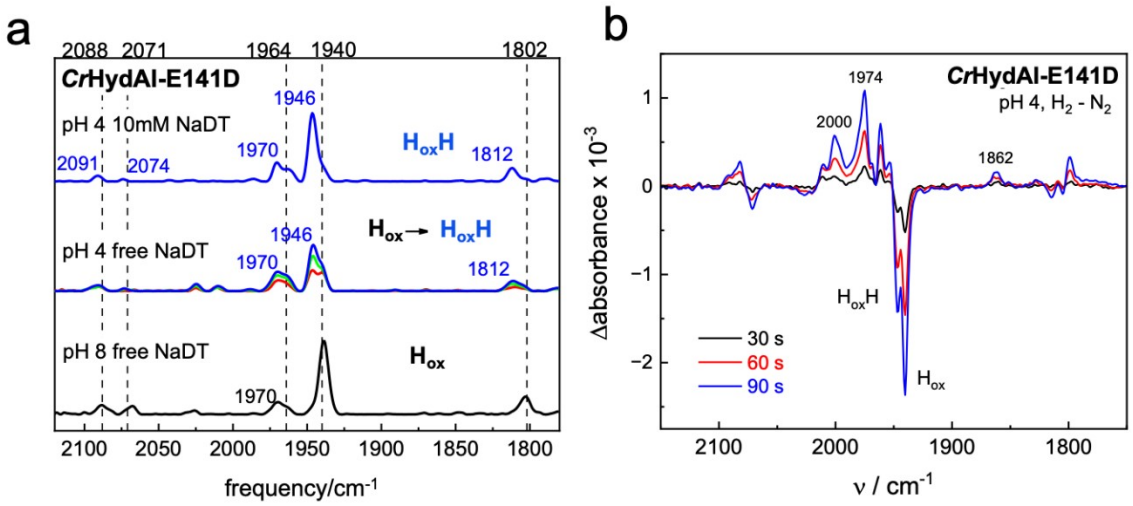

All spectra in panel **(a)** are normalized at 1540 cm^{-1} of the amide II band ahead of baseline correction. N_2 is used to enrich the oxidized states, further conditions are labeled above each spectrum. Upon dehydration of the protein film, *Cr*HydA1-E141D accumulated the $H_{ox}H$ state at pH 4, notably in the absence of NaDT. A similar behavior was observed for *Cp*I-E279D (**Figure S8**). **(b)** Time series of FTIR difference spectra of *Cr*HydA1-E141 (pH 4, no DT) that show the conversion of H_{ox} and $H_{ox}H$ (negative bands) into H_{hyd} or $H_{hyd}H$ as indicated by positive CO bands at 2000, 1974, and 1862 cm^{-1} when the film was reacted with H_2. Compared to wild-type *Cr*HydA1, the signature of the hydride state is shifted to higher frequencies.[3]

Figure S10. FTIR spectroelectrochemistry of *Cr*HydA1.

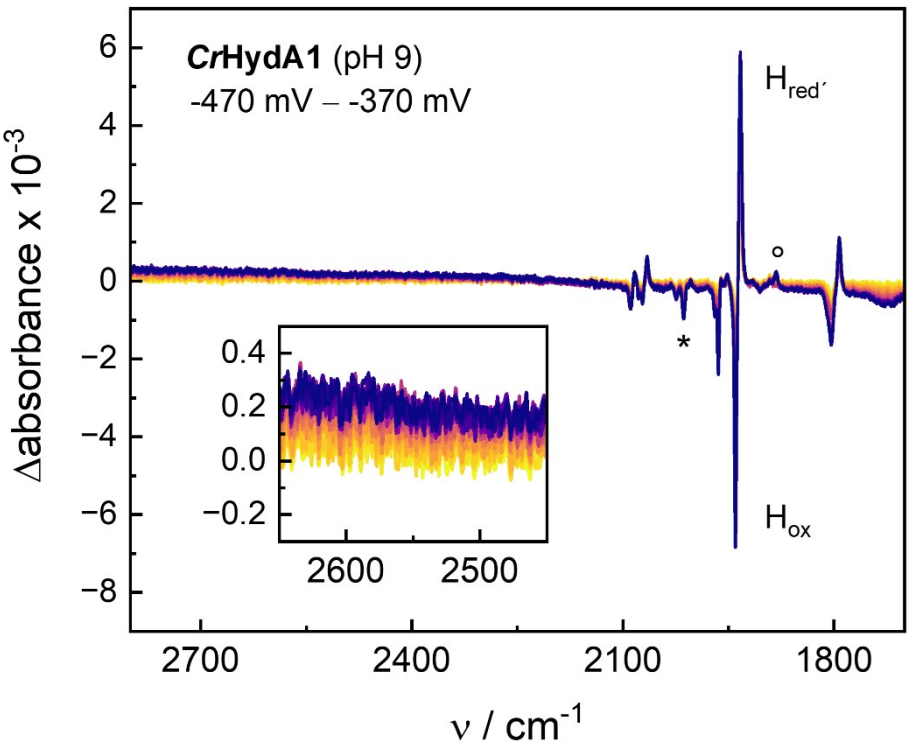

Based on data generated for an earlier publication,[27] we calculated FTIR difference spectra of the electrochemical reduction of *Cr*HydA1. The enzyme was prepared without NaDT and at pH 9. Under these conditions, $H_{red}H^+$ is suppressed and difference spectra allow investigating potential protonation reactions specific for the reduction of $[4Fe]_H$ most of which takes place between -370 mV and -470 mV vs. SHE. Recorded over time after the 100 mV potential jump, the resulting difference spectra are dominated by the H-cluster absorbance changes below 2100 cm^{-1}. Only the main marker bands at 1940 cm^{-1} (H_{ox}) and 1933 cm^{-1} ($H_{red'}$) are labelled. Spectra include insignificant traces of H_{ox}-CO (*) and $H_{red}H^+$ (°). The inset shows the regime between 2650–2450 cm^{-1}. Here, the lack of difference signals around 2550 cm^{-1} is in agreement with a lack of SH protonation changes during the $H_{ox}/H_{red'}$ conversion.[30]

Figure S11. Cluster model used for calculations.

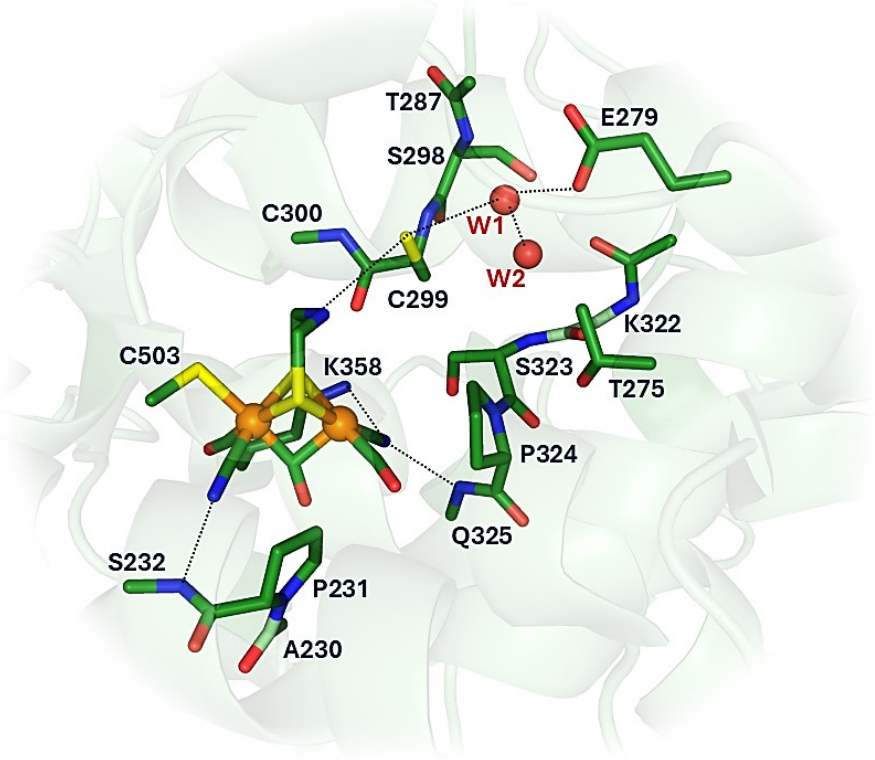

Based on the residue numbering of PDB: 4XDC. Side chains of C299, S298, E279, T275, S323, P324, P231, C503, and K358 were included in the model, along with their contiguous backbone regions where applicable. As for the other residues, only the backbone was accounted for, with truncations applied as necessary. Since the non-rotated form of the H-cluster is thermodynamically more stable in the absence of the protein matrix, it was essential to include residues that stabilize the ligand coordination of the two Fe atoms, ensuring that Fe_d adopts the inverted conformation. To achieve this, we selectively incorporated only the residues directly involved in these interactions, without extending beyond this critical region. We chose not to include the [4Fe-4S] cluster, as our goal was not to precisely match individual experimental spectral bands - an already well-validated approach for computing CO and CN^- stretching frequencies in H-cluster models - but rather to capture the relative shifts in these bands upon protonation of one of the two conserved water molecules (W1 and W2) in the PTP. While omitting the cubane may introduce a minor source of error in the absolute IR frequencies, this effect is expected to remain constant across all simulated systems. As a result, it does not compromise the reliability of our relative comparisons.

Figure S12. Optimized structure obtained by progressively adding one proton starting from an Hox model with hypothetical deprotonated E279.

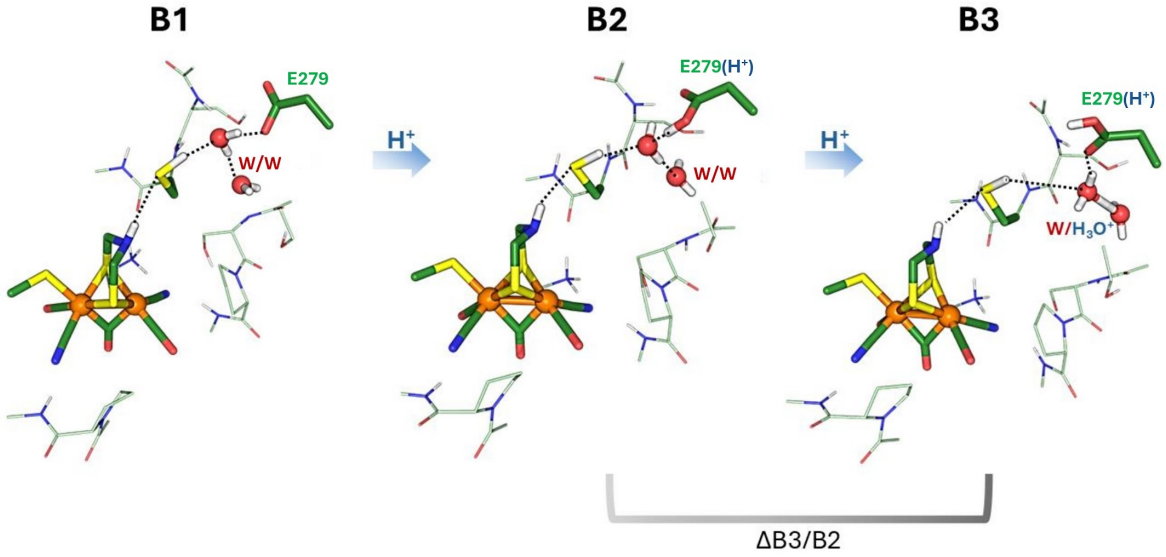

The figure highlights the most stable configuration for structure "B" where the N–H points toward C299 and C299's proton interacts with the lone pair of oxygen of the water molecule. While it is well-known from previous studies that the B configuration is less stable (in this specific case by approximatively 6 to 10 kcal/mol, depending on the protonation state considered), we chose to include it to investigate whether the orientation of protons in the H^+ transfer chain could play a role in the observed blueshift. When starting from E279 configurations (B1), the addition of a first proton to W1/W2, to form a Zundel ion, spontaneously results in the protonation of E279 and the restoration of the two water molecules, yielding structures B2. This state (*i.e.* where E279 is protonated), is the most likely configuration for this site in H_{ox} at pH 7, as previously highlighted based on the peculiar pKa of E279 (8.6), which would reasonably remain protonated under these conditions. Thus, the structures B2 will be used as reference for H_{ox}, to which a second proton will be added to form a Zundel ion (structures B3). The Zundel ion in B3 is stabilized through the formation of multiple hydrogen bonds, involving E279 and the side chain of C299, as well as the backbone of C299 and K322. In these structures, one proton is precisely shared between the two oxygens of W1 and W2.

Figure S13. Predicted shifts of IR bands.

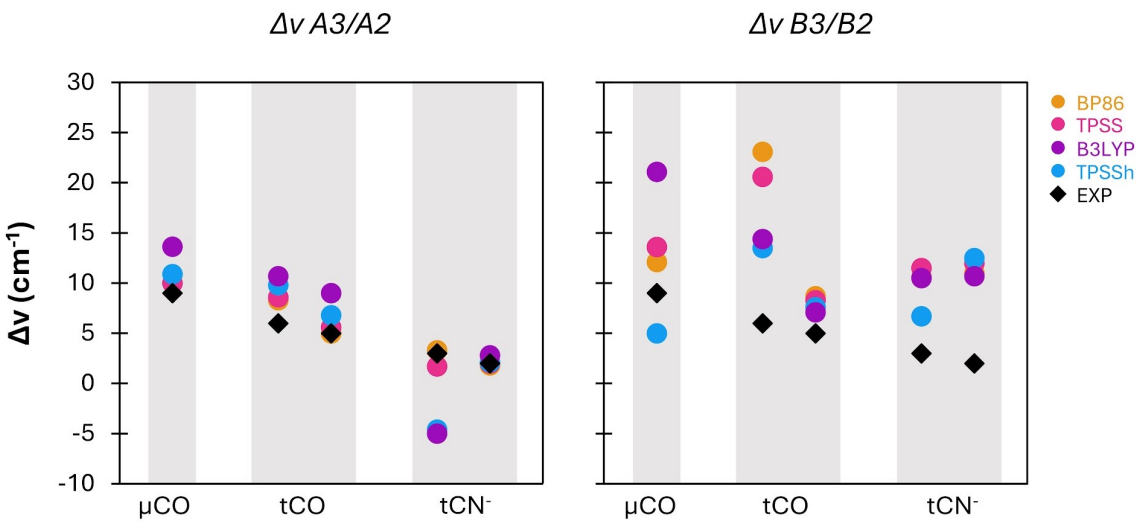

Calculated as vCO/vCN$^-$ of A3 (or B3) minus those of A2 (or B2), so a positive value means a blue shift of bands going from A2 (or B2) to A3 (or B3) using four different levels of theory (two pure functionals: BP86 and TPSS; two hybrids: B3LYP and TPSSh). Structure labels are referred to Figure 4 and S11. For the A configuration (characterized by the NH of the azadithiolate pointing towards Fed, i.e. the most stable and populated conformer), the calculated shifts provide the closest match to the experimental observations. In this case, the average absolute deviation from the experimental shifts is minimal for pure functionals (0.8 cm^{-1} for BP86 and 1.1 cm^{-1} for TPSS) and only slightly larger for hybrid functionals (4.4 cm^{-1} for B3LYP and 3.0 cm^{-1} for TPSSh).

Figure S14. The H-bond analysis with a focus on the regulatory PTP.

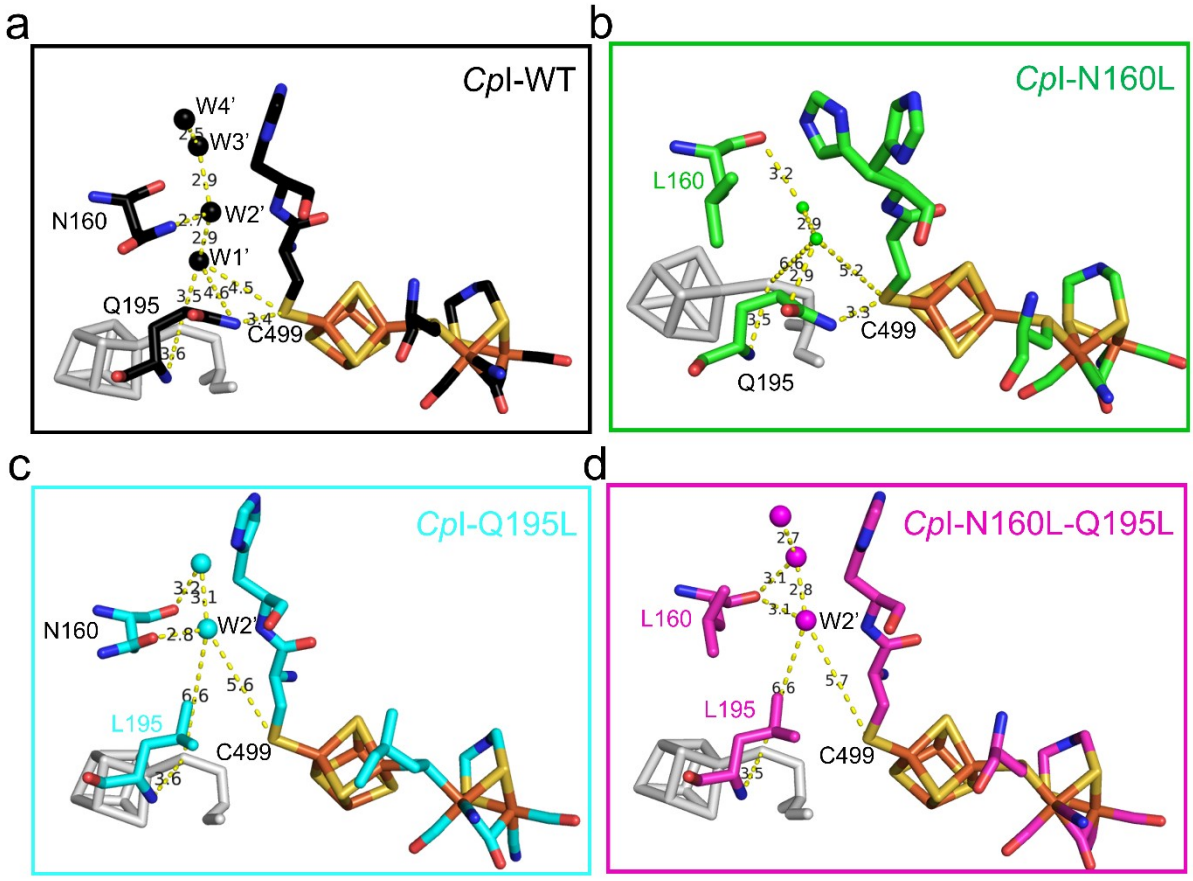

The numbers show the distances in Å between adjacent elements within the regulatory PTPs in each structure.

Figure S15. The H-bond networks of the catalytic PTPs in *Cp*I-E282D, *Cp*I-S319A and *Cp*I-C299D.

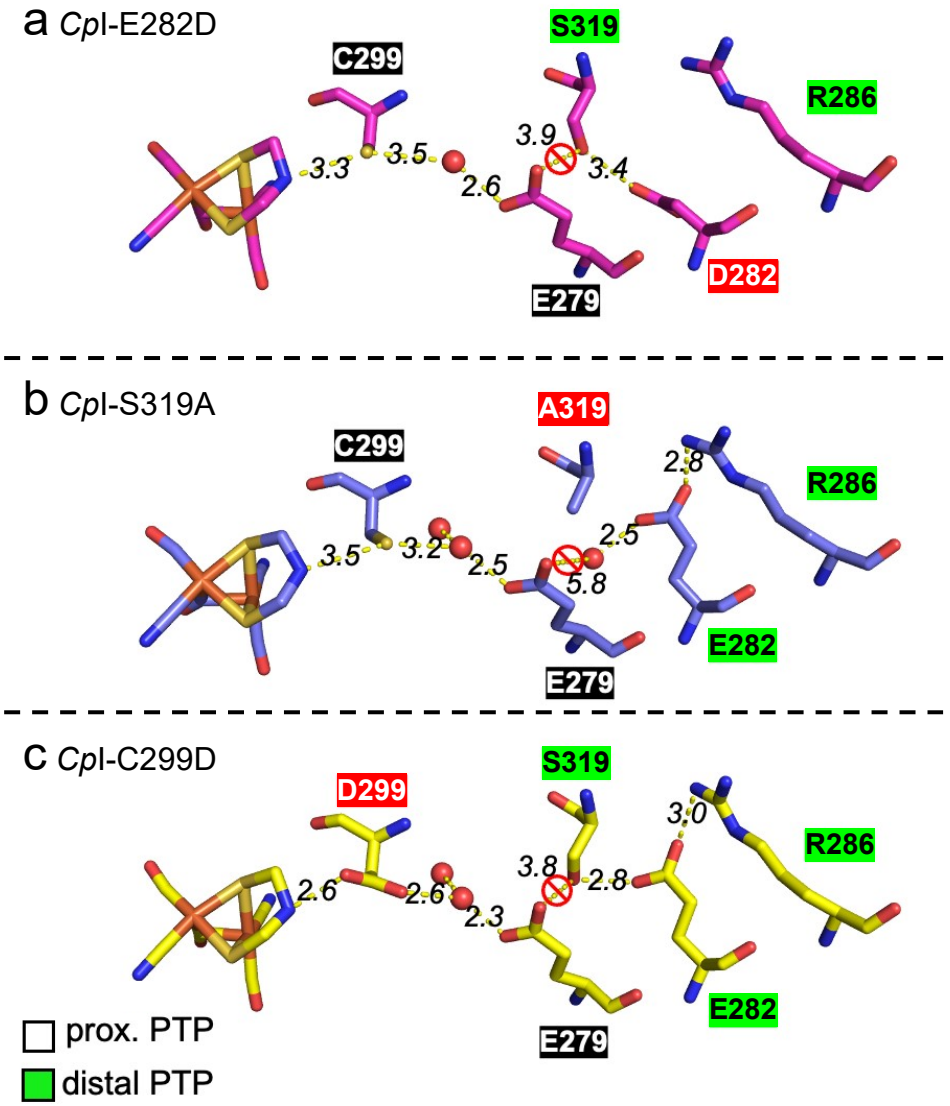

Possible H-bond network along catalytic PTP of chain B of *Cp*I-E282D (a), *Cp*I-S319A (b) and *Cp*I-C299D (c). The dashed lines indicate possible H-bonding interactions, and the distances are shown in Å. The PDB IDs for *Cp*I-E282D, *Cp*I-S319A and *Cp*I-C299D are 6GM2, 6GM4 and 6GLZ respectively.[13]

Supplementary Tables

Table S1. QuikChange PCR primers used for generating *Cp*I variants.

Name	Forward 5'-3'	Reverse 5'-3'
***Cp*I-N160L**	GTGGCAAACTGACTGAAAC CTATGCAATG	TCAGTCAGTTTGCCACAGGC ATTAAC
***Cp*I-Q195L**	GGTTAATGTATCATCGCCTG TCC	ACAGGCGATGATACATTAAC CACAC

Table S2. Calculated RMSD (Å) of the C-α atoms when superimposing the variant structures with 4XDC.

All C-α atoms (566-573) were included in the calculations.

	***Cp*I-N160L**	***Cp*I-Q195L**	***Cp*I-N160L-Q195L**
4XDC (chain A)	0.612	0.736	0.686
4XDC (chain B)	0.357	0.545	0.372

Table S3. Crystallization conditions of *Cp*I variants and used synchrotron facilities.

Name	Buffer	Precipitant	Additives	Salt	Beamline
***Cp*I-N160L**	0.1M Mes pH 6	21% PEG4000	19% Glycerol	0.4M $MgCl_2$	DESY-P13
***Cp*I-Q195L**	0.1M Mes pH 6	21% PEG4000	19% Glycerol	0.4M $MgCl_2$	ESRF-ID23-2
***Cp*I-N160L-Q195L**	0.1M Mes pH 6	20% PEG4000	20% Glycerol	0.4M $MgCl_2$	ESRF-ID23-2

Table S4. X-ray data collection and refinement of crystal structures.

	***Cp*I-N160L**	***Cp*I-Q195L**	***Cp*I-N160L-Q195L**
PDB	**9RJ9**	**9RJQ**	**9RJO**
Data collection			
X-ray wavelength (Å)	0.9795	0.8731	0.8731
Space group	P 1 21 1	P 1 21 1	P 1 21 1
Cell dimension			
a, b, c (Å)	89.66 72.28 102.99	87.79 71.38 103.25	89.15 71.62 102.5
α, β, γ (°)	90.00 97.43 90.00	90.00 101.967 90.00	90.00 97.674 90.00
Resolution (Å)	38.96 - 1.45 (1.502 - 1.45)*	48.11 - 1.75 (1.813 - 1.75)*	47.16 - 1.67 (1.73 - 1.67)*
Rmerge	0.08234 (1.995)*	0.2531 (2.15)*	0.1705 (1.721)*
I / σ(I)	10.58 (1.14)*	5.67 (1.05)*	7.70 (1.06)*
Completeness (%)	99.92 (99.94)*	99.65 (99.85)*	99.79 (99.78)*
Redundancy	6.7 (6.6)*	5.8 (5.5)*	6.6 (6.7)*
CC1/2	0.998 (0.567)*	0.98 (0.278)*	0.999 (0.801)*
Refinement			
Resolution (Å)	38.96 - 1.45	48.11 - 1.75	39.19 - 1.67
No. reflections	230628	125504	148086
Rwork / Rfree	0.1688/0.1908	0.1780/0.2203	0.1782/0.2059
No. atoms			
Protein	9119	8963	9011
Ligand	106	106	106
Water	921	861	758
B-factors			
Protein	31.28	31.35	30.87
Ligand	23.72	22.66	20.81
Water	43.41	40.06	38.40
R.m.s deviations			
Bond lengths (Å)	0.01	0.009	0.009
Bond angles (°)	1.01	1.04	1.02

* Numbers in brackets indicate values in the highest resolution shell.

Table S5. IR band frequencies of CN and CO ligands in *Cp*I and *Cr*HydA1.

State	CN_p	CN_d	CO_p	CO_d	μCO	Reference
			***Cp*I**			
H_{ox}	2081	2068	1970	1947	1801	31,32
$H_{ox}H$	2084	2074	1975	1953	1808	12
$H_{red'}$	2075	2064	1961	1938	1788	this study
$H_{red'}H$	2078	2071	1971	1944	1803	this study
$H_{red}H^+$	2071	2053	1962	1915	1899	33
$H_{sred}H^+$	2065	2039	1958	1922	1894	33
H_{ox}-CO	2090	2076	1973/2015	1969	1807	34
			***Cr*HydA1**			
H_{ox}	2088	2070	1964	1940	1802	35–37
$H_{ox}H$	2092	2074	1970	1946	1812	12
$H_{red'}$	2084	2066	1962	1933	1792	38–40
$H_{red'}H$	2086	2068	1966	1938	1800	12
$H_{red}H^+$	2070	2033	1961	1915	1891	35,36,39
$H_{sred}H^+$	2068	2026	1953	1918	1882	41
H_{ox}-CO	2091	2081	1968	1962	1808	12

References

1 L. Zheng, U. Baumann and J.-L. Reymond, *Nucleic Acids Research*, 2004, **32**, e115.

2 M. K. Akhtar and P. R. Jones, *Appl Microbiol Biotechnol*, 2008, **78**, 853–862.

3 M. Winkler, M. Senger, J. Duan, J. Esselborn, F. Wittkamp, E. Hofmann, U.-P. Apfel, S. T. Stripp and T. Happe, *Nat Commun*, 2017, **8**, 16115.

4 J. M. Kuchenreuther, C. S. Grady-Smith, A. S. Bingham, S. J. George, S. P. Cramer and J. R. Swartz, *PLoS ONE*, 2010, **5**, e15491.

5 H. Li and T. B. Rauchfuss, *J. Am. Chem. Soc.*, 2002, **124**, 726–727.

6 J. Esselborn, C. Lambertz, A. Adamska-Venkatesh, T. Simmons, G. Berggren, J. Noth, J. Siebel, A. Hemschemeier, V. Artero, E. Reijerse, M. Fontecave, W. Lubitz and T. Happe, *Nat Chem Biol*, 2013, **9**, 607–609.

7 J. Duan, A. Veliju, O. Lampret, L. Liu, S. Yadav, U.-P. Apfel, F. A. Armstrong, A. Hemschemeier and E. Hofmann, *J. Am. Chem. Soc.*, 2023, **145**, 26068–26074.

8 G. Goldet, C. Brandmayr, S. T. Stripp, T. Happe, C. Cavazza, J. C. Fontecilla-Camps and F. A. Armstrong, *J. Am. Chem. Soc.*, 2009, **131**, 14979–14989.

9 V. Fourmond, C. Greco, K. Sybirna, C. Baffert, P.-H. Wang, P. Ezanno, M. Montefiori, M. Bruschi, I. Meynial-Salles, P. Soucaille, J. Blumberger, H. Bottin, L. De Gioia and C. Léger, *Nature Chem*, 2014, **6**, 336–342.

10 D. T. Filmon, J. Jaenecke, M. Winkler, V. Fourmond, C. Léger and N. Plumeré, *Proceedings of the National Academy of Sciences*, 2025, **122**, e2514698122.

11 O. Lampret, J. Esselborn, R. Haas, A. Rutz, R. L. Booth, L. Kertess, F. Wittkamp, C. F. Megarity, F. A. Armstrong, M. Winkler and T. Happe, *Proceedings of the National Academy of Sciences*, 2019, **116**, 15802–15810.

12 M. Senger, S. Mebs, J. Duan, O. Shulenina, K. Laun, L. Kertess, F. Wittkamp, U.-P. Apfel, T. Happe, M. Winkler, M. Haumann and S. T. Stripp, *Physical Chemistry Chemical Physics*, 2018, **20**, 3128–3140.

13 J. Duan, M. Senger, J. Esselborn, V. Engelbrecht, F. Wittkamp, U.-P. Apfel, E. Hofmann, S. T. Stripp, T. Happe and M. Winkler, *Nat Commun*, 2018, **9**, 4726.

14 W. Kabsch, *Acta Cryst D*, 2010, **66**, 125–132.

15 P. D. Adams, P. V. Afonine, G. Bunkóczi, V. B. Chen, I. W. Davis, N. Echols, J. J. Headd, L.-W. Hung, G. J. Kapral, R. W. Grosse-Kunstleve, A. J. McCoy, N. W. Moriarty, R. Oeffner, R. J. Read, D. C. Richardson, J. S. Richardson, T. C. Terwilliger and P. H. Zwart, *Acta Cryst D*, 2010, **66**, 213–221.

16 P. Emsley and K. Cowtan, *Acta Cryst D*, 2004, **60**, 2126–2132.

17 A. D. Becke, *Physical review A*, 1988, **38**, 3098.

18 J. P. Perdew, *Phys. Rev. B*, 1986, **33**, 8822–8824.

19 A. Schäfer, C. Huber and R. Ahlrichs, *The Journal of Chemical Physics*, 1994, **100**, 5829–5835.

20 E. Caldeweyher, S. Ehlert, A. Hansen, H. Neugebauer, S. Spicher, C. Bannwarth and S. Grimme, *The Journal of Chemical Physics*, 2019, **150**, 154122.

21 K. Eichkorn, F. Weigend, O. Treutler and R. Ahlrichs, *Theor Chem Acta*, 1997, **97**, 119–124.

22 C. Felbek, F. Arrigoni, D. de Sancho, A. Jacq-Bailly, R. B. Best, V. Fourmond, L. Bertini and C. Léger, *ACS Catal.*, 2021, **11**, 15162–15176.

23 J. Tao, J. P. Perdew, V. N. Staroverov and G. E. Scuseria, *Phys. Rev. Lett.*, 2003, **91**, 146401.

24 V. N. Staroverov, G. E. Scuseria, J. Tao and J. P. Perdew, *The Journal of Chemical Physics*, 2003, **119**, 12129–12137.

25 A. D. Becke, *The Journal of Chemical Physics*, 1993, **98**, 5648–5652.

26 C. Lee, W. Yang and R. G. Parr, *Phys. Rev. B*, 1988, **37**, 785–789.

27 K. Laun, I. Baranova, J. Duan, L. Kertess, F. Wittkamp, U.-P. Apfel, T. Happe, M. Senger and S. T. Stripp, *Dalton Transactions*, 2021, **50**, 3641–3650.

28 O. Lampret, J. Duan, E. Hofmann, M. Winkler, F. A. Armstrong and T. Happe, *PNAS*, 2020, **117**, 20520–20529.

29 M. Senger, J. Duan, M. V. Pavliuk, U.-P. Apfel, M. Haumann and S. T. Stripp, *Inorg. Chem.*, 2022, **61**, 10036–10042.

30 H. Tai, S. Hirota and S. T. Stripp, *Acc. Chem. Res.*, 2021, **54**, 232–241.

31 H. Land, M. Senger, G. Berggren and S. T. Stripp, *ACS Catal.*, 2020, **10**, 7069–7086.

32 J. H. Artz, O. A. Zadvornyy, D. W. Mulder, S. M. Keable, A. E. Cohen, M. W. Ratzloff, S. G. Williams, B. Ginovska, N. Kumar, J. Song, S. E. McPhillips, C. M. Davidson, A. Y. Lyubimov, N. Pence, G. J. Schut, A. K. Jones, S. M. Soltis, M. W. W. Adams, S. Raugei, P. W. King and J. W. Peters, *J. Am. Chem. Soc.*, 2020, **142**, 1227–1235.

33 J. Khushvakov, R. Nussbaum, C. Cadoux, J. Duan, S. T. Stripp and R. D. Milton, *Angewandte Chemie International Edition*, 2021, **60**, 10001–10006.

34 S. Morra, J. Duan, M. Winkler, P. A. Ash, T. Happe and K. A. Vincent, *Dalton Trans.*, 2021, **50**, 12655–12663.

35 A. J. Pierik, M. Hulstein, W. R. Hagen and S. P. J. Albracht, *European Journal of Biochemistry*, 1998, **258**, 572–578.

36 S. P. J. Albracht, W. Roseboom and E. C. Hatchikian, *J Biol Inorg Chem*, 2006, **11**, 88–101.

37 M. Senger, S. Mebs, J. Duan, F. Wittkamp, U.-P. Apfel, J. Heberle, M. Haumann and S. T. Stripp, *Proceedings of the National Academy of Sciences*, 2016, **113**, 8454–8459.

38 A. Adamska-Venkatesh, D. Krawietz, J. Siebel, K. Weber, T. Happe, E. Reijerse and W. Lubitz, *J. Am. Chem. Soc.*, 2014, **136**, 11339–11346.

39 C. Sommer, A. Adamska-Venkatesh, K. Pawlak, J. A. Birrell, O. Rüdiger, E. J. Reijerse and W. Lubitz, *J. Am. Chem. Soc.*, 2017, **139**, 1440–1443.

40 S. Katz, J. Noth, M. Horch, H. S. Shafaat, T. Happe, P. Hildebrandt and I. Zebger, *Chemical Science*, 2016, **7**, 6746–6752.

41 A. Adamska, A. Silakov, C. Lambertz, O. Rüdiger, T. Happe, E. Reijerse and W. Lubitz, *Angewandte Chemie International Edition*, 2012, **51**, 11458–11462.